Density Compensated Thermohaline Gradients and Diapycnal Fluxes in the Mixed Layer

LIANGGUI CHEN AND W. R. YOUNG

Scripps Institution of Oceanography, La Jolla, California

(Manuscript received 18 October 1994, in final form 24 March 1995)

ABSTRACT

Density-compensated temperature and salinity gradients are often observed in mixed layer fronts. A possible explanation of this observation is that there is a systematic relation between the "strength" of a front, defined as the buoyancy jump across the front, and the thickness of a front. If stronger fronts tend to be thicker, then in an ensemble of random fronts, in which the temperature and salinity jumps are independent random variables, the temperature and salinity gradients will be correlated. This correlation between the thermohaline gradients is such that heat and salt make antagonistic contributions to the buoyancy gradient—that is, there is buoyancy compensation. The statistics of heat and salt fluxes across nearly compensated fronts are counterintuitive: strong heat fluxes can occur across a front with weak thermal gradients and strong salinity gradients, and vice versa.

As a specific model that relates the width of a front to the strength of a front, a pair of coupled nonlinear diffusion equations for heat and salt are used. The nonlinear diffusion coefficient, proportional to the square of the buoyancy gradient, arises from quasi-steady shear dispersion driven by thermohaline gradients. This nonlinear mixing prevents stirring by mesoscale advection from indefinitely filamenting mixed layer tracer distributions. The model predicts that the thickness of a front varies as the square root of the strength and inversely as the one-quarter power of the mesoscale strain.

1. Introduction

The mixed layer (ML) density field is often characterized by "density compensation" between temperature and salinity gradients. Often these compensated thermohaline features are found in the individual fronts that make up "frontal zones." An example is the subarctic frontal zone in the North Pacific: the observations of Roden (1977) and Yuan and Talley (1992) contain abundant examples of fronts with temperature and salinity gradients that nearly cancel in their joint effect on density. Figure 1 shows the top 100 m of the Marathon II (152°W) CTD section. In the subarctic frontal zone, at around 42°N, there is considerable structure in the salinity and temperature fields that has no expression in the density field. In the North Pacific subtropical frontal zone the observations of Samelson and Paulson (1988) show a sequence of fronts, many of which have some degree of compensation. In the subantarctic frontal zone of the Argentine Basin, Roden's (1986) Fig. 12 shows another example of remarkable density compensation in the ML.

One explanation of these observations is that atmospheric forcing conspires to create and juxtapose water masses with nearly compensating properties. A more satisfactory explanation is the upper-ocean frontogenesis model of MacVean and Woods (1980). These authors use an oceanographic version of the model of Hoskins and Bretherton (1972). MacVean and Woods show that for some initial conditions the isotherm and isohaline patterns make a front appear to be much thinner and deeper than does the isopycnal pattern.

The solution of Hoskins and Bretherton ignores turbulent mixing of heat, salt, and momentum. Because of these idealizations the model predicts singularities in which density gradients and vorticity become infinite in a finite time. In this article we turn to the question of the dissipation, which arrests the formation of the singularity and produces a front with a finite width. The mechanism we discuss is shear dispersion driven by horizontal buoyancy gradients. This dissipative process is nonlinear because the shear dispersion coefficient is proportional to the square of the velocity (Taylor 1953) and the velocity is proportional to the horizontal buoyancy gradient.

2. Thermohaline shear dispersion in the mixed layer

Dissipation in the ML is the result of processes that span many decades of length scales. In this section we formulate a model, which is intended to resolve thermohaline structure with horizontal length scales on the order of 1 km to 10 km and timescales longer than a few inertial periods. Motions that have smaller lengths and higher frequencies than this (e.g., Langmuir circulations and shear flow instabilities) are parameter-

Corresponding author address: Dr. Lianggui Chen, Scripps Institution of Oceanography, University of California, San Diego, 9500 Gilman Drive, La Jolla, CA 92093.
E-mail: Chen@dalek.ucsd.edu

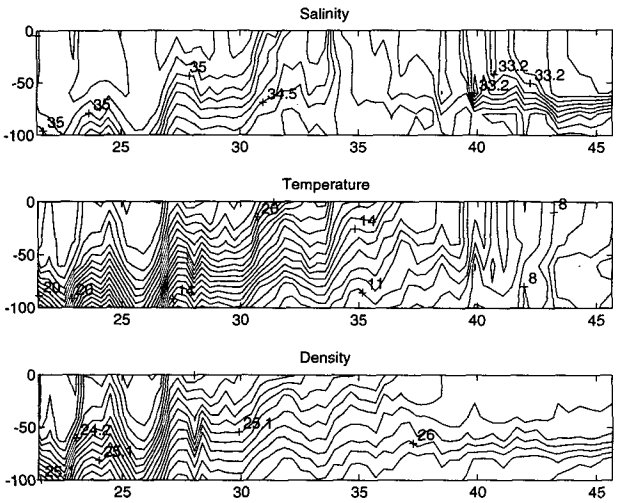

FIG. 1. Salinity (S), temperature (T), and density (σ_t) in the upper 100 m of the Marathon II (115°W) CTD section in the North Pacific. The subarctic frontal zone is at around 41°N. The units are constructed so that the contour intervals in the three panels correspond to comparable jumps in density.

ized as "mixing." In particular, all of the mixing processes that maintain the vertical homogeneity of the ML against the shear driven restratification discussed by Tandon and Garrett (1994) and Young (1994) are lumped into this mixing.

The mixing parameterization we introduce below is a nonlinear, downgradient diffusivity for heat and salt. The nonlinear diffusion arises because the horizontal transport of heat and salt is by shear dispersion, and the shear flow doing the dispersing is driven by the horizontal buoyancy gradient (e.g., Young 1994). Thus, the strength of the shear dispersion increases as the horizontal buoyancy gradients become larger—in fact, the diffusion coefficient is proportional to the square of the buoyancy gradient.

The complement to mixing is "stirring" (e.g., Eckart, 1948). Because of the relatively small scale of ML fronts the mesoscale eddy field can be modeled as advection by a velocity field whose length scale is much larger than that of the front: this prescribed advection is "stirring." A popular idealization of mesoscale deformation is

$$u = \chi x, \quad v = -\chi y, \tag{2.1}$$

(e.g., Garrett 1983; Hoskins and Bretherton 1972; MacVean and Woods 1980; Young et al. 1982). The typical rate of mesoscale strain, χ, can be estimated by supposing that there is 10 cm s^{-1} difference in velocity over a distance of 100 km so that $\chi \sim 10^{-6}\ s^{-1}$.

In adopting the velocity field in (2.1) we have in mind a ML front embedded in an externally imposed mesoscale strain field. The Cartesian coordinate system in (2.1) translates with the front and is aligned with the principal axes of the rate of strain tensor (e.g., Batchelor 1958).

The simplest model combining mesoscale stirring with shear dispersive mixing is coupled advection–diffusion equations for the vertically averaged ML temperature and vertically averaged ML salinity:

$$S_t - \chi y S_y = (DS_y)_y, \quad T_t - \chi y T_y = (DT_y)_y, \tag{2.2a,b}$$

where $T(y, t)$ is the ML temperature and $S(y, t)$ is the ML salinity. In (2.2) D is a positive definite diffusivity, which depends nonlinearly on the buoyancy gradient: this is mixing by shear dispersion. Thus, making the approximation that the equation of state is linear, the ML buoyancy is

$$B(y, t) = g\alpha_T T(y, t) - g\alpha_S S(y, t), \tag{2.3}$$

and two models for the nonlinear diffusivity in (2.2) are

$$D_1(B_y) = \gamma |B_y|, \quad D_2(B_y) = \gamma B_y^2. \tag{2.4a,b}$$

For expositional purposes we also consider the linear case in which D is uniform.

If one forms an appropriate linear combination of (2.2a) and (2.2b), then one can write a single closed equation for the evolution of the ML buoyancy $B(y, t)$ in (2.3). Once this equation has been solved, one can turn to (2.2a) and (2.2b) individually. Thus, in this paper we do not consider processes that break the dynamical symmetry between T and S (e.g., thermal feedback between the atmosphere and the ocean or the large-scale effects of double diffusion).

The parameterization in (2.4a) is the transfer law proposed by Stommel (1961, 1993): if one takes a two grid-point discretization of (2.2) with (2.4a) and sets $\chi = 0$, then one recovers Stommel's two-box model with its "capillary flow" rule in which the exchange is proportional to the absolute value of the pressure difference between the two boxes. The partial differential equation in (2.2) can be thought of as a continuum of coupled boxes and in this sense (2.2) is a development toward higher resolution of Stommel's model.

The parameterization in (2.4b) is a representation of thermohaline shear dispersion. This nonlinear diffusivity, increasing with the square of the buoyancy gradient, is one of the ML processes described by the subinertial mixed layer (SML) approximation. The SML approximation is a filtering of the three-dimensional equations of motion (Young 1993). The independent variables of the SML approximation are the vertically averaged salinity $S(x, y, t)$, the vertically averaged temperature $T(x, y, t)$, and the streamfunction for the vertically averaged velocity $\psi(x, y, t)$. If these three fields have spatial variation in only one direction ($\partial_x = 0$) and $\psi = -\chi xy$, then the SML approximation reduces to (2.2) and (2.4b).

The collapse of the SML approximation to the coupled nonlinear diffusion equations in (2.2) is to be ex-

pected on the basis of experience with nonrotating problems involving density-driven shear dispersion. This problem was first addressed by Erdogan and Chatwin (1967) and was reviewed by Young and Jones (1991). The thermohaline case, in which the density is jointly determined by heat and salt, was previously discussed by Cessi and Young (1992).

The cubically nonlinear diffusion law in (2.4b) results from a frictionally balanced, density-driven shear flow transporting the buoyancy field down its own gradient. The down-pressure-gradient velocity is linearly proportional to the horizontal pressure gradient which, in turn, is linearly proportional to the horizontal buoyancy gradient. But the shear dispersion coefficient varies as the square of the velocity (Taylor 1953) so that the effective diffusivity in (2.4b) is proportional to the square of the horizontal buoyancy gradient.

In the case of unidirectional variation the effect of rotation is confined to the expression for γ in (2.4b):

$$\gamma \equiv \frac{1}{12}\mu^2(1+\mu^2)^{-2}(\tau\mathcal{H}^2/f^2) \tag{2.5}$$

(Young 1994). In (2.5) $\mathcal{H}$ is the undisturbed depth of the ML, f is the Coriolis parameter, τ is the timescale for the vertical mixing of heat and salt, and μ is a nondimensional parameter

$$\mu = \frac{1}{f\tau_U}, \tag{2.6}$$

where τ_U is the timescale for the vertical mixing of momentum in the ML. If the vertical mixing is modeled with an eddy viscosity ν and an eddy diffusivity κ, then $\tau \sim \mathcal{H}^2/\kappa$ and $\tau_U \sim \nu/\mathcal{H}^2$. The nonrotating limit is recovered from (2.5) by taking the limit $\mu \to \infty$ so that $\gamma \approx \mathcal{H}^2\tau_U^2\tau/12 \sim \mathcal{H}^8/\nu^2\kappa$ [cf. Eq. (39) in Young and Jones (1991)].

As nominal numerical values, suppose that the ML depth is $\mathcal{H} \approx 100$ m and that $f \approx 10^{-4}$ s^{-1} while $\tau \approx \tau_U \approx 10^5$ s. In this case $\mu \approx 1/10$ and $\gamma \approx 10^{14}$ m^2 s^3. This estimate of γ is used throughout this paper. We emphasize that γ is not a uniquely defined constant but rather depends on adopting the "relaxation" time denoted by τ. Roughly speaking, τ is the interval between the mixing events that vertically homogenize the mixed layer. In the sequel, the crucial assumption is that the various parameters in (2.5) are independent of the horizontal buoyancy gradient B_y. This ensures that the dependence of the nonlinear diffusivity in (2.4b) on the horizontal buoyancy gradient is $D \sim B_y^2$.

A buoyancy gradient is estimated using the value $\Delta T \approx 0.4$°C over $\Delta y \approx 1$ km observed by Samelson and Paulson (1988) in the North Pacific subtropical frontal zone. With $\alpha_T \approx 2.5 \times 10^{-4}\,K^{-1}$ the buoyancy gradient is

$$B_y \approx g\alpha_T\frac{\Delta T}{\Delta y} \approx 10^{-6}\ \text{s}^{-2}. \tag{2.7}$$

With these figures the order of magnitude of the nonlinear diffusivity in (2.4b) is

$$D = \gamma B_y^2 \approx 10^2\ \text{m}^2\ \text{s}^{-1}. \tag{2.8}$$

This is a very large diffusivity for a submesoscale process, and we emphasize that we have used a horizontal buoyancy gradient in (2.7) that is characteristic of frontal regions. Because of the quadratic dependence in (2.4b) the diffusivity is much smaller outside of frontal zones.

It is interesting to contrast the order of magnitude of the ML diffusivity in (2.8) with an estimate of the shear dispersion diffusivity due to internal waves in the ocean interior. In the interior regime, Young et al. (1982) estimated that the oscillatory velocity fields of internal waves produce a horizontal diffusivity about 1000 times the vertical diffusivity. Using the recently measured order of magnitude 10^{-5} m^2 s^{-1} for the interior vertical diffusivity (Ledwell et al. 1993) gives a horizontal diffusivity of order 10^{-2} m^2 s^{-1}. This interior horizontal diffusivity is smaller by a factor of 10^4 than the ML diffusivity in (2.8).

3. Thermohaline fronts

In this section we turn to the solution of (2.2) and the statistical implications of this solution for a frontal zone comprising an ensemble of fronts. The main point here is that if a front exists with large gradients in temperature and salinity then, in order for the front not to diffuse away, the temperature and salinity gradients must make antagonistic contributions to the buoyancy gradient. This reasoning needs a few qualifications, which we make in section 5.

a. The width of a front: The balance between advection and diffusion

Consider a configuration like that in Fig. 2 where a thermohaline front is created by the deformation field in (2.1) pushing together two water masses with different salinities and temperatures. The frontal boundary

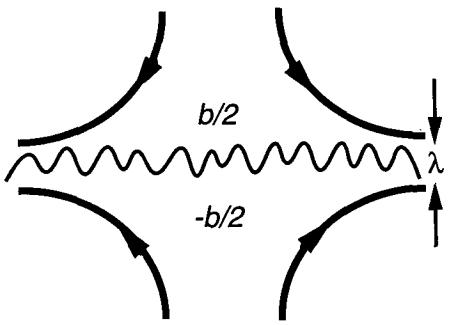

FIG. 2. A sketch of a thermohaline front of thickness λ formed by the deformation field in (2.1) pushing two water masses with different properties together.

between the two masses has a thickness that reflects the competition between advection and diffusion. For instance, if the diffusivity D in (2.2) is constant, then this frontal scale is

$$\lambda_{\text{linear}} \equiv \left(\frac{D}{\chi}\right)^{1/2} \tag{3.1}$$

(e.g., Garrett 1983). Notice that with this linear model the thickness of the front is independent of the buoyancy jump across it.

Now consider what happens with the nonlinear diffusivity in (2.4b): the balance between advection and nonlinear diffusion is established when the thickness of the front is of order

$$\lambda \equiv \left(\frac{\gamma}{\chi}\right)^{1/4} |b|^{1/2}, \tag{3.2}$$

where b is the buoyancy jump across the front. We refer to $|b|$ as the "strength" of the front. The result in (3.2) can be established with dimensional reasoning and it is supported by a detailed calculation in appendix A.

The implication of (3.2) is that with the nonlinear diffusivity stronger fronts are also thicker fronts. The exact dependence of thickness on strength is model dependent: with the alternative model in (2.4a) the result analogous to (3.2) is $\lambda \sim |b|^{1/3}$. Throughout this paper we use (3.2) because the SML approximation provides a physical justification for the antecedent (2.4b). But the main conclusions apply to all models in which there is a systematic relation between the thickness of a front and the strength of a front. The relation between thickness and strength is a nontrivial result of thermohaline shear dispersion: (3.1) shows that if the diffusivity is linear then thickness is independent of strength.

To estimate an order of magnitude for λ in (3.2) we use our previous estimates that $\gamma \sim 10^{14}$ m^2 s^3 and $\chi \sim 10^{-6}$ s^{-1}. If the buoyancy jump corresponds to 1 K, then $b \sim 2.5 \times 10^{-3}$ m s^{-2} and $\lambda \sim 5$ km. The buoyancy gradient is $b/\lambda \sim 5 \times 10^{-7}$ s^{-2} $\sim 50 f^2$.

We now turn to the consequences of (3.2) for the thermohaline gradients. As measures of the salinity and temperature jumps across the front, we introduce

$$\sigma \equiv g\alpha_S \Delta S, \quad \theta \equiv g\alpha_T \Delta T \tag{3.3}$$

so that the buoyancy jump is $b = \theta - \sigma$. The gradients within the front then scale with

$$f \equiv \frac{\sigma}{\lambda} = \chi^{1/4}\gamma^{-1/4}|\theta - \sigma|^{-1/2}\sigma,$$

$$g \equiv \frac{\theta}{\lambda} = \chi^{1/4}\gamma^{-1/4}|\theta - \sigma|^{-1/2}\theta,$$

$$h \equiv \frac{b}{\lambda} = \chi^{1/4}\gamma^{-1/4}\,\text{sgn}(\theta - \sigma)|\theta - \sigma|^{1/2}. \tag{3.4a,b,c}$$

The final equation (3.4c) shows that the buoyancy gradient, $h = g - f$, scales with the square root of the strength $|b|$. But the salinity and temperature gradients, f and g in (3.4a,b), do not have a simple dependence on $|b|$. In Fig. 3 we show some isolines of constant salinity gradient, f, in the (σ, θ) plane.

b. An ensemble of random fronts

Now imagine creating an ensemble of "random fronts" by selecting points in the (σ, θ) plane of Fig. 3 according to some simple probability density function. [Below in (3.5) we use a Gaussian density function centered on the origin.] The ensemble of fronts generated by such a procedure has a smooth distribution of widths, λ, and buoyancy gradients, h, because neither of these quantities are subject to large fluctuations when a point near the line $b = 0$ is selected.

But if one picks a point very near to the $b = 0$ line in the θ–σ plane, then there are large fluctuations in f and g, which have no expression in λ and h: a point near the $b = 0$ line corresponds to a very weak density front, which is also very thin because $\lambda \sim |b|^{1/2}$. This must be a density compensated front in the sense that there are large and antagonistic gradients of temperature and salinity: these two gradients are large simply because weak density fronts are systematically thinner than strong density fronts. This is the essential physics in (3.2) and this is what produces the "near-zero divisors" in (3.4a) and (3.4b).

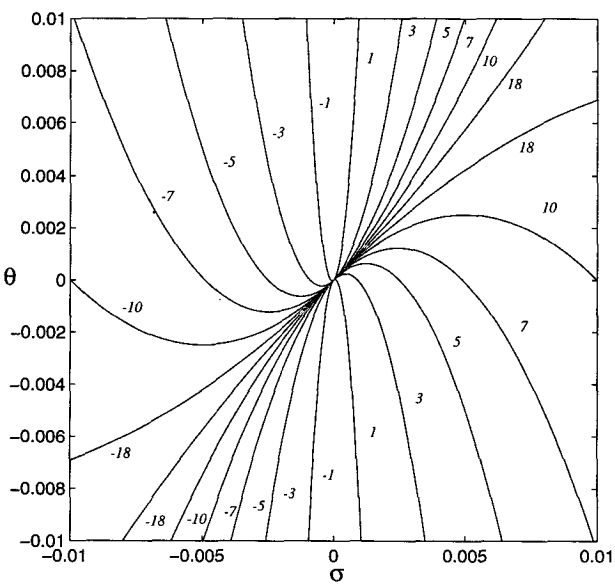

FIG. 3. Some contours of constant salinity gradient, f, in the σ, θ plane calculated from (3.4a) with $\gamma = 10^{14}$ m^2 s^3 and $\chi = 10^{-6}$ s^{-2}. Both σ and θ are in the buoyancy units (m s^{-2}) defined in (3.3). The contours of f are labeled in units 10^{-6} s^{-2}.

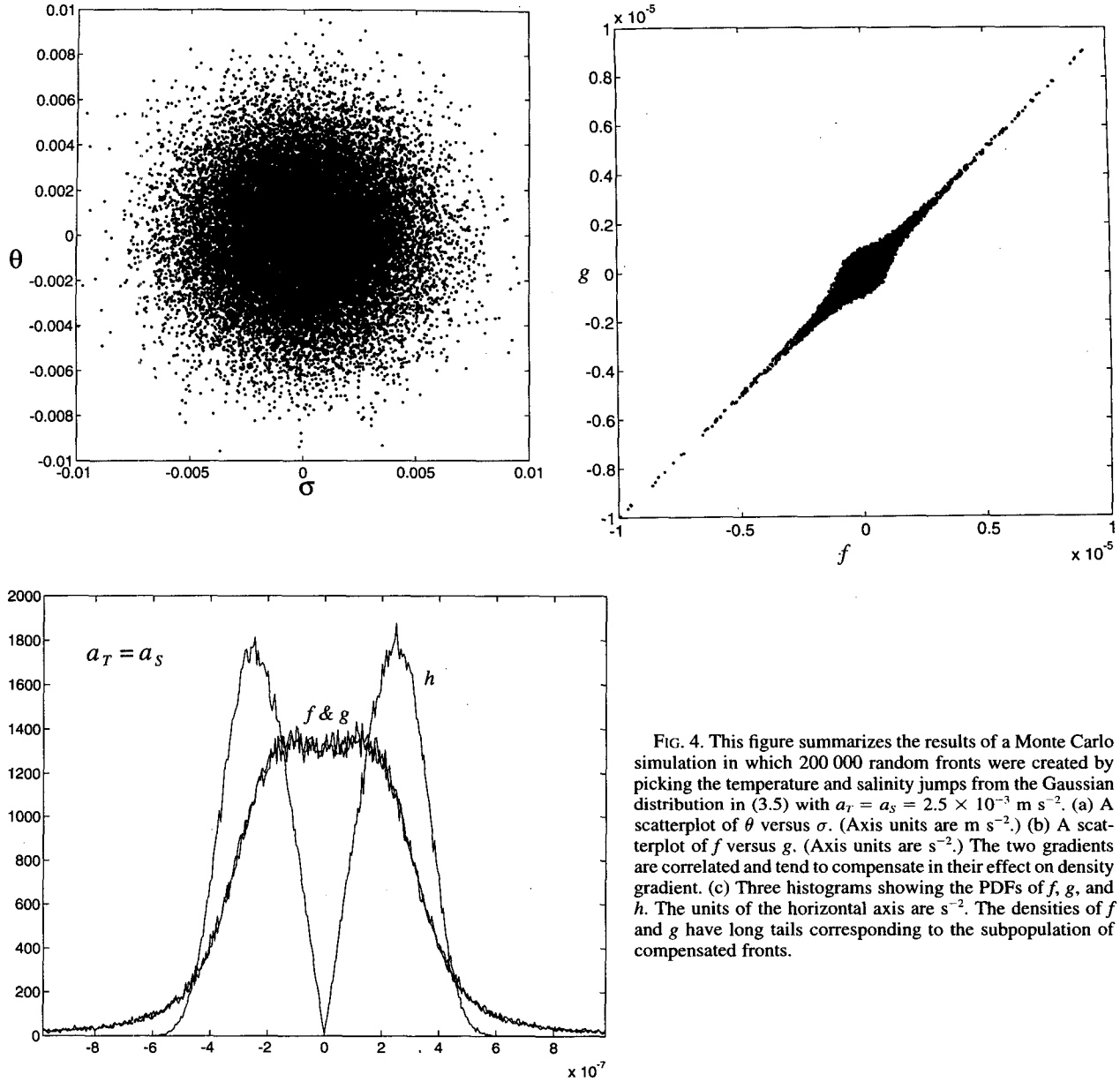

FIG. 4. This figure summarizes the results of a Monte Carlo simulation in which 200 000 random fronts were created by picking the temperature and salinity jumps from the Gaussian distribution in (3.5) with $a_T = a_S = 2.5 \times 10^{-3}$ m s^{-2}. (a) A scatterplot of θ versus σ. (Axis units are m s^{-2}.) (b) A scatterplot of f versus g. (Axis units are s^{-2}.) The two gradients are correlated and tend to compensate in their effect on density gradient. (c) Three histograms showing the PDFs of f, g, and h. The units of the horizontal axis are s^{-2}. The densities of f and g have long tails corresponding to the subpopulation of compensated fronts.

We illustrate this argument with a Monte Carlo simulation in which the thermohaline jumps are selected from a Gaussian distribution

$$\mathcal{P}(\sigma, \theta) = \frac{1}{2\pi a_S a_T} \exp\left(-\frac{\sigma^2}{2a_S^2} - \frac{\theta^2}{2a_T^2}\right), \quad (3.5)$$

where a_S and a_T are the rms fluctuations in σ and θ. If the rms fluctuation in the temperature jump is 1 K, then $a_T = 2.5 \times 10^{-3}$ m s^{-2}. We adopt this as our standard case and initially suppose that $a_S = a_T$ so temperature and salinity make equal contributions to the density. We also use $\gamma = 10^{14}$ m^2 s^3 and $\chi = 10^{-6}$ s^{-1} as standard values in what follows.

In Fig. 4 we show the result of selecting 200 000 random points according to the prescription in the paragraph above. Figure 4a shows the density of points in the (σ, θ) plane. There is little to say except that the random number generator works: there are no correlations between the temperature and salinity jumps, and there are exponentially few "outliers" in this Gaussian cloud of points. Figure 4b is a scatterplot showing the temperature and salinity gradients f and g defined in (3.4a,b). The clustering along the compensation line $f = g$ is obvious. Thus, even though there are no correlations between the temperature and salinity jumps in Fig. 4a, the temperature and salinity gradients in Fig.

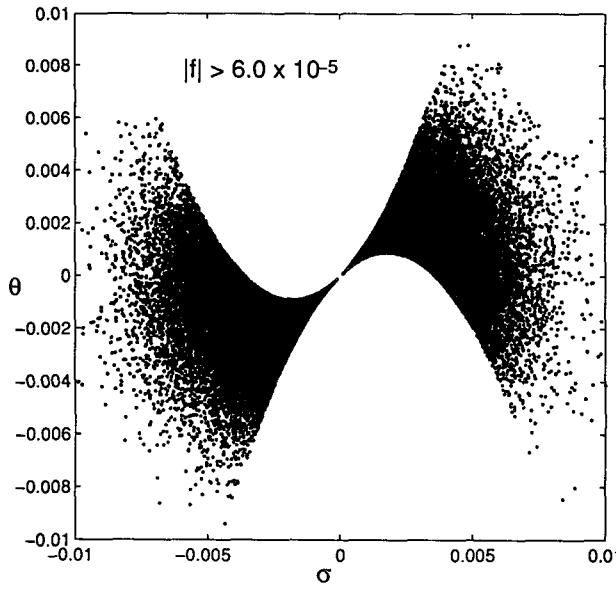

FIG. 5. A scatterplot of σ versus θ for the subpopulation of fronts with $|f| > 6 \times 10^{-5}\ s^{-2}$. These fronts, with very strong temperature gradients, correspond to points that cluster along the line $\sigma = \theta$ as one approaches the origin of the plane.

3b are correlated and tend to cancel in their joint effect on buoyancy gradient. Figure 4c shows the probability density functions (PDFs) of the three random gradients f, g, and h.

Consider the very strong fronts in Fig. 4c. The histogram shows that there are few representatives in the ensemble with buoyancy gradients, h, as large as $6 \times 10^{-7}\ s^{-2}$. But there are some fronts whose temperature and salinity gradients individually are larger than $6 \times 10^{-7}\ s^{-2}$. These are the large fluctuations produced when a point falls near the $b = 0$ line in the σ, θ plane. Figure 5 shows the results of selecting from the ensemble of 200 000 random fronts the subpopulation with $|f| > 6 \times 10^{-7}\ s^{-2}$ and then scatterplotting these 51 294 points in the θ–σ plane. The result is consistent with the argument above: this subpopulation of very strong salinity fronts clusters along the $b = \theta - \sigma = 0$ line. More precisely, points with a large salinity gradient, say $|f|$ greater than some specified threshold, lie between the constant f contours shown in Fig. 3. The origin of the (σ, θ) is a point of singularity of the function $f(\sigma, \theta)$ so there is a finite possibility of having large values of the salinity gradient, f, right at the peak of the Gaussian distribution in (3.5). A more quantitative characterization is given in appendix B.

The results in Figs. 4 and 5 were based on an ensemble of random fronts in which temperature and salinity fluctuations make equal contributions to the buoyancy fluctuations. In Fig. 6 we show that the main conclusions are unchanged if the two tracers make unequal contributions. We constructed another ensemble of 200 000 random fronts but in the Gaussian density (3.5) we took $a_T = 2a_S = 5.0 \times 10^{-3}\ m\ s^{-2}$ so that the temperature jumps are twice as strong as the salinity jumps. This is evident in the θ–σ scatterplot in Fig. 6a. Figure 6b shows the scatterplot of the thermohaline gradients f and g. Again there is an obvious correlation along the compensation line. Figure 6c shows the PDF of the three gradients. Comparing this figure with the PDFs, Fig. 3c, we notice that the PDF of the buoyancy gradient, h, is unchanged apart from a rescaling. However, in Fig. 5c the PDF of the temperature gradient, g, begins to resemble the PDF of the buoyancy gradient h. This is what one would anticipate as the temperature jumps become stronger. However, equally striking is the long tail representing large salinity and temperature gradients with no accompanying buoyancy gradients; for example, there are very few representatives in the ensemble with $|h| > 7 \times 10^{-7}\ s^{-2}$. Also striking is that for these large fluctuations the PDFs of the temperature gradient f and the salinity gradient g are identical even though $a_T = 2a_S$. This is another indication that virtually every very strong temperature front is also a very strong salinity front with compensation between the two fields.

We also experimented with non-Gaussian PDF for θ and σ and found that the main conclusions are unaltered: the PDFs of f and g have long tails, which represent a subpopulation of density compensated fronts.

c. *The statistics of thermohaline gradients*

All of the results in the previous subsection can be explained with a straightforward and tedious calculation of the various PDFs of λ, f, g, and h. The results are collected in appendix B. The most significant of these results are those in (B12) and (B13):

$$\mathcal{P}(f) \sim |f|^{-3}, \quad \mathcal{P}(g) \sim |g|^{-3}, \quad (3.6a,b)$$

where $\mathcal{P}$ is the probability density function and where the approximations apply if $|f|$ and $|g|$ are large. Thus, the tail of large salinity and temperature fronts in Figs. 4c and 6c has a power law decay. Because of these large fluctuations the rms salinity and temperature gradients are infinite: the integral $\int f^2 \mathcal{P}(f)\, df$ diverges. Thus, the statistics of thermohaline gradients are intermittent (there are very large fluctuations) even though the statistics of thermohaline jumps are Gaussian.

One final point concerns the detailed structure of the joint PDF of (f, g). Figure 7 shows the data from Fig. 4b plotted in a rotated and anisotropically scaled set of coordinates. (Some outliers on the horizontal axis are not shown.) Figure 7 shows that characterizing the temperature and salinity gradients as "compensated" is accurate only for the large gradients. The extension of the cloud along the vertical axis $(f + g = 0)$ shows that small gradients are actually "anticompensated." Also evident in Fig. 7 is the void right on the compensation line where $g - f = 0$. This empty region is explained by the prefactor $(f - g)^2$ on the right-hand

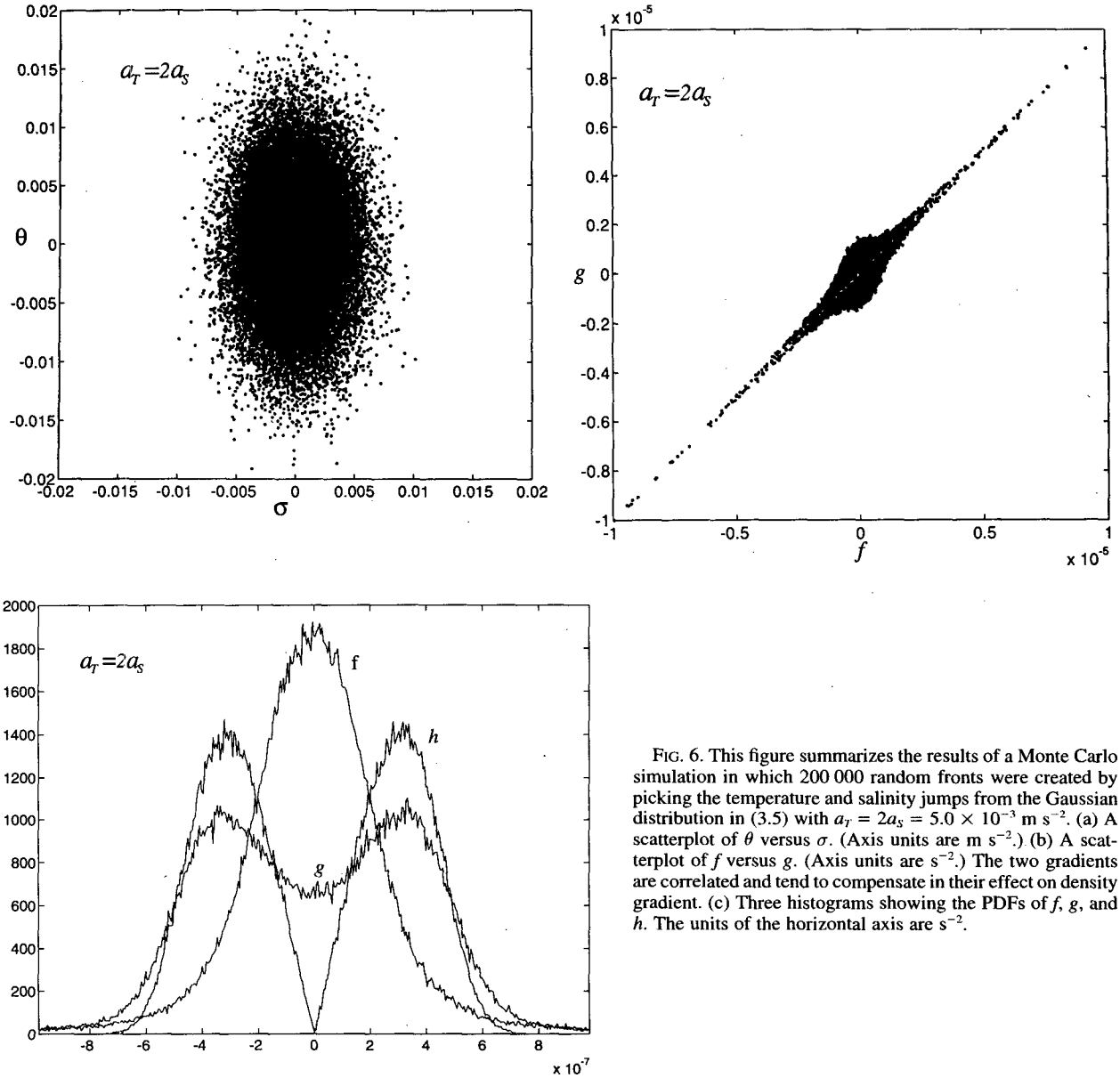

FIG. 6. This figure summarizes the results of a Monte Carlo simulation in which 200 000 random fronts were created by picking the temperature and salinity jumps from the Gaussian distribution in (3.5) with $a_T = 2a_S = 5.0 \times 10^{-3}$ m s^{-2}. (a) A scatterplot of θ versus σ. (Axis units are m s^{-2}.) (b) A scatterplot of f versus g. (Axis units are s^{-2}.) The two gradients are correlated and tend to compensate in their effect on density gradient. (c) Three histograms showing the PDFs of f, g, and h. The units of the horizontal axis are s^{-2}.

side of (B8): the PDF vanishes when $f - g = 0$. But nonetheless, the large fluctuations cluster in two mountains on either side of this valley because the exponential factor in (B8) has its largest value when $f - g = 0$.

4. Fluxes in the mixed layer

The salinity flux in our model is

$$F_S = \chi y S - \gamma B_y^2 S_y, \tag{4.1}$$

where the first term on the rhs is advection and the second term is nonlinear diffusion. If we evaluate this flux at $y = 0$ (the center of the front), then the advective contribution vanishes, and the remainder is the downgradient diffusive flux of salt through the center of the front. This cross-frontal flux is tending to equalize the salinities of the two water masses in Fig. 2. Using our previous estimates of the thermohaline gradients in (3.4), we see that $F_S \sim \gamma h^2 f$. This motivates the introduction of three new variables:

$$p \equiv -\gamma h^2 f = -\gamma^{1/4}\chi^{3/4}|\theta - \sigma|^{1/2}\sigma$$

$$q \equiv -\gamma h^2 g = -\gamma^{1/4}\chi^{3/4}|\theta - \sigma|^{1/2}\theta$$

$$r \equiv -\gamma h^3 = -\gamma^{1/4}\chi^{3/4}\,\mathrm{sgn}(\theta - \sigma)|\theta - \sigma|^{3/2} \tag{4.2a,b,c}$$

that are measures of the salt, heat, and buoyancy fluxes through the front.

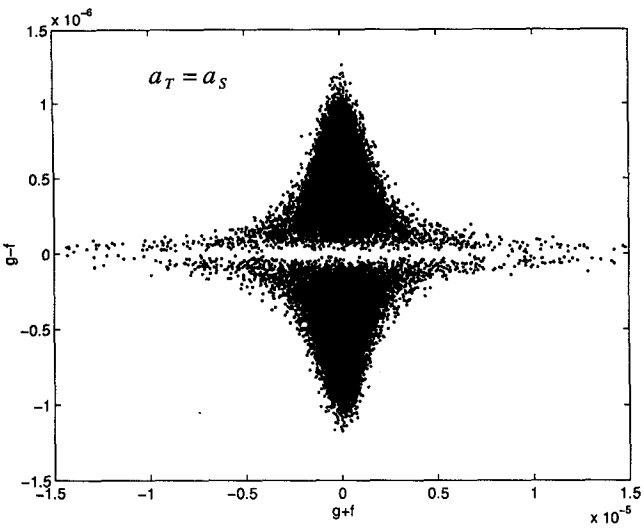

FIG. 7. A detailed view of the thermohaline gradient plane in Fig. 4b. (Axis units are m s^{-2}.) The axes have been rotated and scaled anisotropically to show the void along the line $g - f = 0$.

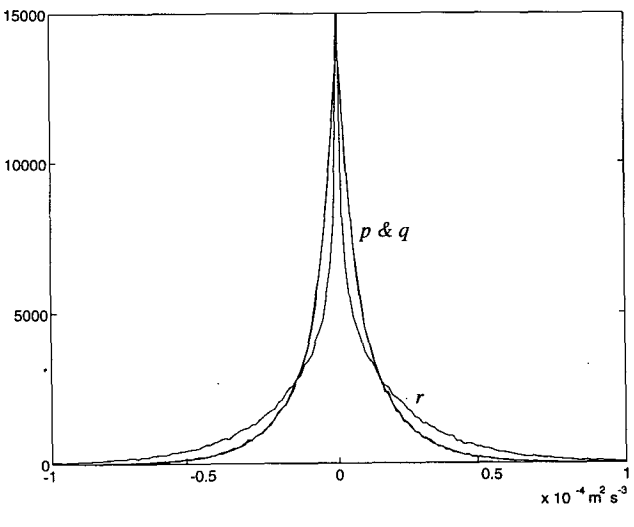

FIG. 8. Histograms of the three fluxes defined in (4.2) (the units of the horizontal axis are m^2 s^{-3}). The Monte Carlo simulation is the same as in Fig. 4.

To estimate the size of these fluxes suppose that the temperature jump across the front is 1° and there is no salinity compensation so that $b = 2.5 \times 10^{-3}$ m s^{-2}. Using $\gamma \sim 10^{14}$ m^2 s^3 and $\chi \sim 10^{-6}$ s^{-1} gives $\lambda \sim 5$ km and $r \sim 10^{-5}$ m^2 s^{-3}.

There are no divisors in the definitions in (4.2), so we anticipate that in an ensemble of random fronts the fluxes, unlike the gradients, will not have large fluctuations. This expectation is confirmed by both the Monte Carlo simulation in Fig. 8 and the analytic calculation in appendix B. Figure 8 shows the PDFs of the three random fluxes constructed using the same set of 200 000 random fronts used in Fig. 4. The calculation of the PDFs in appendix B confirms the impression from Fig. 8 that large fluctuations in the fluxes are exponentially rare.

This result in Fig. 8, if true of the ocean, has important consequences for models of the large-scale circulation. If the statistics of fluxes are relatively well behaved, then it makes sense to associate diapycnal fluxes in the mixed layer with an "average front." This is in contrast to the intermittent statistics that characterize heat and salt gradients in the middle of fronts. Nonetheless, although the flux statistics are not intermittent, their dependence on the jumps in heat and salt across the front are nonintuitive: without some theoretical model the relations in (4.2) are not obvious.

The statistical consequences of (4.2) seem paradoxical if one attempts to correlate fluxes with gradients. For instance, in Fig. 9 we show a scatterplot of the heat flux, q, versus the temperature gradient g. All 200 000 points fall in the second and fourth quadrants because flux, q, and gradient, g, have opposite signs [see (4.2b)]. But the correlation has nothing else in common with the results from a linear model. The vertical arm of the cross in Fig. 9a shows that weak temperature gradients can be associated with strong heat fluxes while the horizontal arm shows the reverse. Thus, there is a correlation between weak heat fluxes and strong

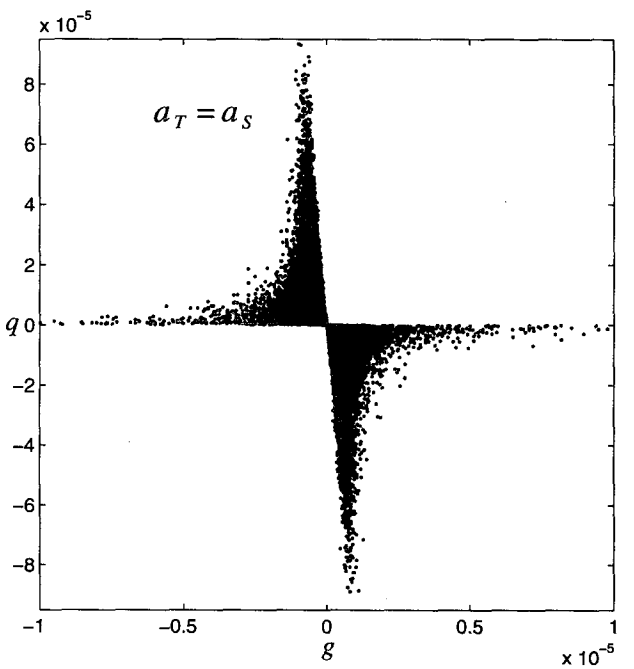

FIG. 9. A scatterplot of the heat flux, q, versus the temperature gradient, g, for the Monte Carlo simulation in Fig. 4. The points lie on a cross indicating that there are two possible correlations: strong fluxes associated with weak gradients (the vertical arm) and weak fluxes associated with strong gradients (the horizontal arm).

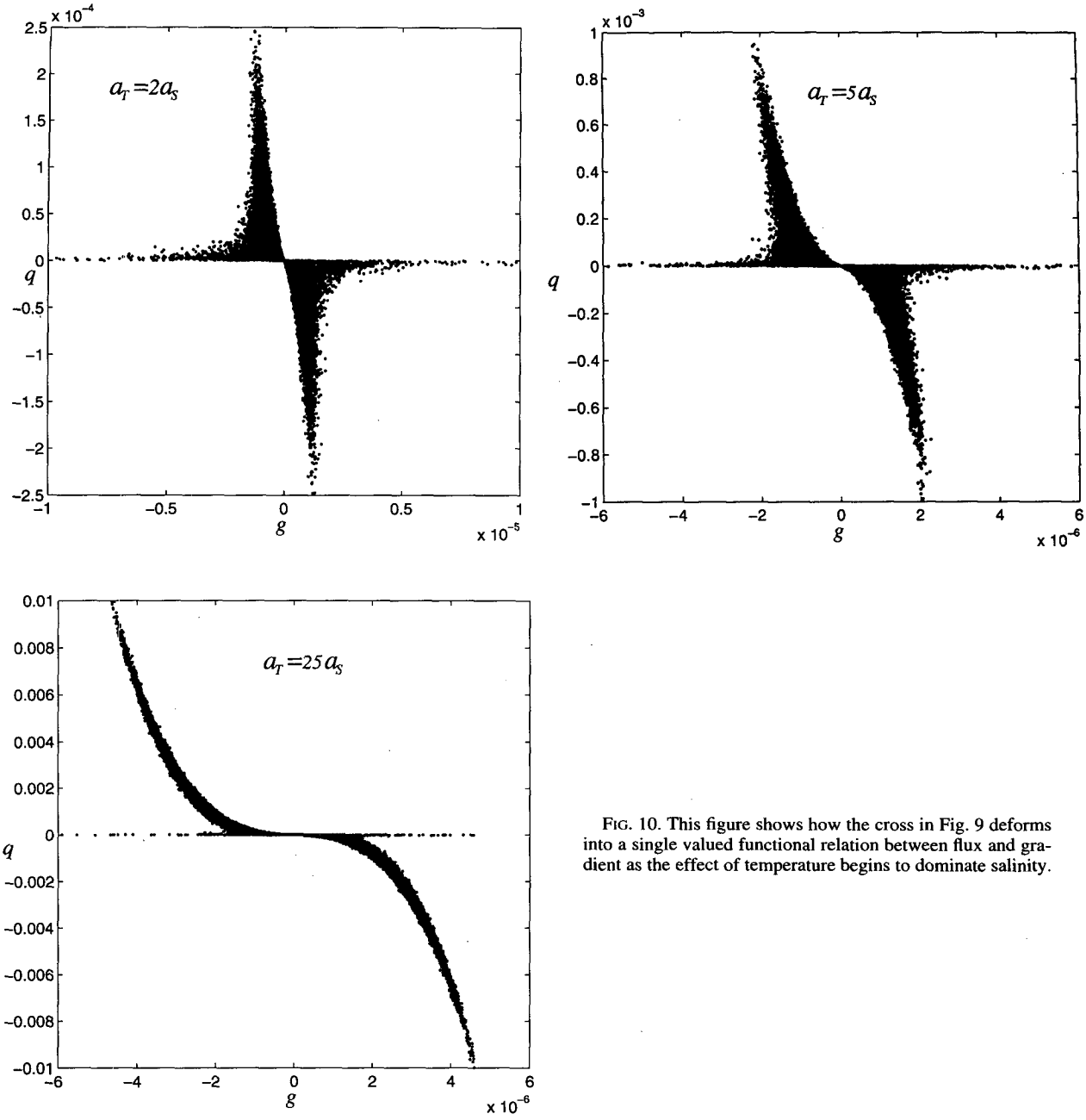

FIG. 10. This figure shows how the cross in Fig. 9 deforms into a single valued functional relation between flux and gradient as the effect of temperature begins to dominate salinity.

temperature gradients, and vice versa! The key to all this is the salinity.

The extreme points on the vertical arm of the cross in Fig. 9 are characterized by rather small values of θ and larger values of σ with the opposite sign to θ; that is, the buoyancy gradient is dominated by salinity and the weaker temperature gradient reinforces the salinity. Thus these points on the vertical arm are strong fronts dominated by salinity. Although θ is small, the heat flux q in (4.2b) can be large because the factor $|\theta - \sigma|^{1/2}$ is large. If one's primary interest is modeling or measuring ML heat fluxes, then this is a compelling reason for directing attention at strong salinity fronts. (And, of course, vice versa.)

The extreme points on the horizontal arm of the cross in Fig. 9 are the buoyancy compensated fronts in which the salinity and temperature gradients are large but antagonistic. Thus, in this case, the factor $|\theta - \sigma|^{1/2}$ in (4.2b) is very small so that the heat flux q is small. To summarize: the largest temperature fronts are buoyancy compensated by salinity and very little heat diffuses across these regions of high temperature gradient.

A scatterplot of buoyancy flux, r, against buoyancy gradient, h, is a "semicubic" curve because from (4.2c) these two variables are functionally related. This leads one to enquire how the cross in Fig. 9 deforms to the single-valued relation in (4.2c) as one increases the strength of the temperature jump θ relative to the salinity jump σ. In Fig. 10 we show a scatterplot of q versus g when a_T ranges from $2a_S$ to $25a_S$. The slow deformation of the cross into the single-valued functional relation in (4.2c) is clear.

5. Discussion

In this paper we have proposed a statistical explanation for the observation of density compensated fronts in the ML. The theory has two logically distinct components:

(i) There is relation such as (3.2) between the strength and the thickness of a front.

(ii) The laws for the transformation of probabilities then imply that thermohaline gradients are correlated.

The physical content of the theory is entirely in (i) and it is here that we have appealed to thermohaline shear dispersion, parameterized as a nonlinear diffusivity in (2.4b), to justify (3.2). But other physical models might lead to (3.2), and from that point forward the calculations involved in (ii) are unchanged.

For instance, as an example of an alternative argument that leads to a relation between the thickness and strength of a front, suppose that there is a reduced-gravity g' at the base of the ML. Further, suppose that the front thickness, λ, is proportional to the deformation radius of the ML:

$$\lambda \sim \sqrt{g'\mathcal{H}}/f. \tag{5.1}$$

If one argues that a substantial fraction of the isopycnals peel off the base of the ML and outcrop at the front, then $|b| \sim g'$, and we arrive at $\lambda \sim |b|^{1/2}$, as in (3.2), by an entirely different route. But the subsequent implications of $\lambda \sim |b|^{1/2}$ for the statistics of thermohaline gradients are the same as those shown in Figs. 4 through 7. This is the content of point (ii) above.

The reasoning in the paragraph above makes no reference to nonlinear diffusivity or shear dispersion. Thus it is not necessarily the case that the compensation we have described in this paper occurs because a front with large gradients in temperature and salinity diffuses away unless these thermohaline gradients largely cancel in their joint effect on buoyancy gradient. It is our opinion that such a process of diffusive selection likely acts in ML frontal zones. But we emphasize that the relation between frontal strength and frontal thickness is the essential physics and that the same relation can arise from entirely different models.

In section 4 we showed that thermohaline shear dispersion makes some interesting predictions concerning the relations between fluxes and gradients in the ML. The main point here is that the buoyancy gradient determines the size of the diapycnal transports. If one considers only the temperature gradient, and ignores salinity, then it is difficult to reach any useful conclusion about the diapycnal heat flux (e.g., Fig. 9). This is in contrast to the usual linear model in which heat fluxes are proportional to temperature gradients.

Acknowledgments. We are grateful for the support of the National Science Foundation under OCE93-01462 and the CHAMMP program (DOE DEFG03 93ER61690). We thank Daniel Rudnick for useful conversations during the course of this research.

APPENDIX A

Details of the Front Solution

In this appendix we collect the details of the frontal solution used in section 3. We begin by introducing the functions

$$\eta \equiv e^{\chi t} y$$
$$\tau \equiv \frac{1}{4\chi}\left(e^{4\chi t} - 1\right) \tag{A1a,b}$$

and using (η, τ) as independent coordinates instead of (y, t). The transformation rules

$$\partial_y = e^{\chi t}\partial_\eta$$
$$\partial_t = e^{4\chi t}\partial_\tau + \chi\eta\partial_\eta \tag{A2a,b}$$

can then be used to rewrite (2.2) and (2.4b) as

$$S_\tau = \gamma(B_\eta^2 S_\eta)_\eta, \quad T_\tau = \gamma(B_\eta^2 T_\eta)_\eta. \tag{A3a,b}$$

Thus, the transformation in (A1) folds the effects of advection into a coordinate change.

The transformed Eq. (A3) has a similarity solution that represents the diffusion of a front (Smith 1982):

$$g\alpha_S S_\eta = \frac{\sigma}{c\tau^{1/4}}\frac{2}{\pi}\sqrt{1-\xi^2}, \quad \text{if} \quad |\xi| < 1$$

$$g\alpha_T T_\eta = \frac{\theta}{c\tau^{1/4}}\frac{2}{\pi}\sqrt{1-\xi^2}, \quad \text{if} \quad |\xi| < 1, \tag{A4a,b}$$

and if $|\xi| > 1$, then $T_\eta = S_\eta = 0$. In Eqs. (A4) the similarity variable is

$$\xi \equiv \frac{\eta}{c\tau^{1/4}}, \tag{A5}$$

and the constants θ and σ are the jump in temperature and salinity across the front expressed in buoyancy units [see (3.3)]. Thus the jump in buoyancy across the front is

$$b \equiv \theta - \sigma, \tag{A6}$$

and the constant c is defined by

$$c^4 \equiv \frac{48}{\pi^2}\gamma b^2. \tag{A7}$$

In terms of the original variables (y, t), one has

$$\sigma = \int_{-l}^{l} S_\eta d\eta, \quad \theta = \int_{-l}^{l} T_\eta d\eta, \tag{A8a,b}$$

where $l(t)$ is the width of the front:

$$l(t) = e^{-\chi t} c\tau^{1/4} = \left(\frac{12}{\pi^2}\frac{\gamma}{\chi}b^2\right)^{1/4}(1 - e^{-4\chi t})^{1/4}. \tag{A9}$$

Because $l(0) = 0$, this solution shows how an initial discontinuity is smoothed by the nonlinear diffusion. When $4\chi t \gg 1$, the front reaches its equilibrium thickness, which is very nearly equal to the length λ in (3.2).

APPENDIX B

The Transformation of Probability Density Functions

In this appendix we collect the calculations required to obtain the probability density functions (PDFs) of the three gradient f, g, and h defined in (3.4) and the width λ defined in (3.2). We begin by noting that if the jumps in temperature and salinity are given by the Gaussian PDF in (3.5) then the PDF of the buoyancy jump $b = \theta - \sigma$ is also Gaussian:

$$\mathcal{P}(b) = \frac{1}{\sqrt{2\pi}a_B}\exp\left(-\frac{b^2}{2a_B^2}\right), \tag{B1}$$

where $a_B^2 = a_S^2 + a_T^2$ is the rms buoyancy jump. In this appendix we use $\mathcal{P}$ to denote a PDF and the argument of $\mathcal{P}$ will indicate the random variable to which we are refering.

One can calculate the PDF of λ defined in (3.2) using the rule for transformation of probabilities:

$$\mathcal{P}(\hat{\lambda}) = \sum \mathcal{P}(b)\left|\frac{db}{d\hat{\lambda}}\right| = 4\pi^{-1/2}\hat{\lambda}\exp(-\hat{\lambda}^4)H(\hat{\lambda}), \tag{B2a,b}$$

where $\hat{\lambda} \equiv (\chi/2\gamma a_B^2)^{1/4}\lambda$ is a nondimensional front width and $H(\hat{\lambda})$ is the Heaviside step function. The $\sum$ in (B2a) is because $\lambda \sim |b|^{1/2}$ so that one must account for the two branches, $b > 0$ and $b < 0$, that map to the same $\lambda > 0$.

In the same fashion one can calculate the PDF of the buoyancy gradient:

$$\mathcal{P}(\hat{h}) = 2\pi^{-1/2}\hat{h}\exp(-\hat{h}^4), \tag{B3}$$

where $\hat{h} = (\gamma/2\chi a_B^2)^{1/4}h$ is a nondimensional buoyancy gradient. Both of the PDFs in (B2) and (B3) decay very quickly as their arguments become large. This exponential decay ensures that all moments exist. For instance, for the buoyancy gradient,

$$\langle|\hat{h}|^n\rangle \equiv \int_{-\infty}^{\infty}|\hat{h}|^n\mathcal{P}(\hat{h})d\hat{h} = \pi^{-1/2}\Gamma\left(\frac{n+2}{4}\right). \tag{B4a,b}$$

Putting $n = 2$ in the formula above and restoring the dimensions, we see that the rms buoyancy gradient is $(2\chi a_B^2/\gamma\pi)^{1/4}$.

To calculate the joint PDF of the gradients f and g, we begin by noting that the definitions in (3.4) imply

$$\sigma = (\gamma/\chi)^{1/2}f(g - f)\,\mathrm{sgn}(g - f)$$
$$\theta = (\gamma/\chi)^{1/2}g(g - f)\,\mathrm{sgn}(g - f). \tag{B5a,b}$$

One now regards (B5) as a mapping from the (f, g) plane to the (σ, θ) plane. The Jacobian of this mapping is

$$\frac{\partial(\sigma, \theta)}{\partial(f, g)} = 2(\gamma/\chi)(g - f)^2. \tag{B6}$$

The transformation rule, which gives the joint PDF of f and g in terms of the Gaussian PDF of σ and θ in (2.5), is

$$\mathcal{P}(f, g) = \mathcal{P}(\sigma, \theta)\left|\frac{\partial(\sigma, \theta)}{\partial(f, g)}\right|. \tag{B7}$$

The mapping in (B5) and (B6) applied to the Gaussian PDF in (3.5) gives

$$\mathcal{P}(\hat{f}, \hat{g}) = \frac{4}{\pi}\csc(2\varphi)(\hat{g} - \hat{f})^2\exp[-(\hat{f} - \hat{g})^2 \times (\sec^2(\varphi)\hat{f}^2 + \csc^2(\varphi)\hat{g}^2)]. \tag{B8}$$

In (B8), φ is

$$\varphi \equiv \arctan(a_T/a_S), \tag{B9}$$

and the nondimensional gradients are

$$(\hat{f}, \hat{g}, \hat{h}) \equiv (\gamma/2\chi a_B^2)^{1/4}(f, g, h). \tag{B10}$$

The angle $\pi/2 > \varphi > 0$ is a nondimensional measure of the relative contributions of the temperature and salinity to the thermohaline gradients.

The marginal density of salinity gradients is

$$\mathcal{P}(f) = 4\pi^{-1}\csc(2\varphi)\int_{-\infty}^{\infty}d\hat{g}(\hat{g} - \hat{f})^2 \times \exp[-(\hat{f} - \hat{g})^2(\sec^2(\varphi)\hat{f}^2 + \csc^2(\varphi)\hat{g}^2)]$$
$$= 4\pi^{-1}\csc(2\varphi)\int_{-\infty}^{\infty}du\,u^2\exp[-u^2(\sec^2(\varphi)\hat{f}^2 + \csc^2(\varphi)(u + \hat{f})^2)]. \tag{B11a,b}$$

We were unable to find a convenient analytic simplification of the integral in (B11b). But if $|\hat{f}| \gg 1$, then the integrand is strongly peaked round $u = 0$ and Laplace's method gives the asymptotic expansion

$$\mathcal{P}(\hat{f}) \sim \frac{\pi^{3/2}}{4} \sin^2(2\varphi)\hat{f}^{-3}, \quad \text{if} \quad \hat{f} \gg 1. \quad \text{(B12)}$$

An analogous calculation gives the asymptotic behavior of the marginal distribution of temperature gradients:

$$\mathcal{P}(\hat{g}) \sim \frac{\pi^{3/2}}{4} \sin^2(2\varphi)\hat{g}^{-3}, \quad \text{if} \quad \hat{g} \gg 1. \quad \text{(B13)}$$

Note that in this asymptotic limit the two PDFs are equal no matter what the value of φ.

Whereas the PDF of the buoyancy gradients in (B3) decays exponentially, the PDFs of the salinity and temperature gradients in (B11) and (B12) decay only algebraically. This relatively slow decay means that the average,

$$\langle |\hat{f}|^n \rangle \equiv \int |\hat{f}|^n \mathcal{P}(\hat{f}) d\hat{f}, \quad \text{(B14)}$$

diverges if $n \geq 2$. Thus the rms salinity and temperature gradients are infinite while the rms buoyancy gradient is finite.

We turn now to the PDFs of the fluxes p, q, and r defined in (4.2). The easiest is the buoyancy flux for which

$$\mathcal{P}(\hat{r}) = \frac{2}{3}\pi^{-1/2}|\hat{r}|^{-1/3} \exp(-|\hat{r}|^{4/3}), \quad \text{(B15)}$$

where $\hat{r} = 2^{-3/4}a_B^{-3/2}\gamma^{-1/4}\chi^{-3/4}r$ is a nondimensional buoyancy flux. The PDF in (B15) has an integrable singularity at $\hat{r} = 0$ but it decays exponentially if $|\hat{r}| \gg 1$.

To calculate the joint PDF of (p, q), we begin by noting that the inverse of the relations in (4.2a) and (4.2b) is

$$\sigma = -\gamma^{-1/6}\chi^{-1/2}|p - q|^{-1/3}q$$
$$\theta = -\gamma^{-1/6}\chi^{-1/2}|p - q|^{-1/3}p. \quad \text{(B16a,b)}$$

The equations above define a mapping from the (p, q) plane to the (σ, θ) plane. The Jacobian is

$$\frac{\partial(\sigma, \theta)}{\partial(p, q)} = -\frac{2}{3}\gamma^{-1/3}\chi^{-1}|p - q|^{-2/3}, \quad \text{(B17)}$$

so that the transformation analogous to (B7) gives

$$\mathcal{P}(\hat{p}, \hat{q}) = \frac{4}{3\pi}\csc(2\varphi)|\hat{p} - \hat{q}|^{-2/3} \exp[-|\hat{p} - \hat{q}|^{-2/3} \times (\sec^2(\varphi)\hat{q}^2 + \csc^2(\varphi)\hat{p}^2)], \quad \text{(B18)}$$

where the nondimensional fluxes are

$$(\hat{p}, \hat{q}, \hat{r}) \equiv 2^{-3/4}a_B^{-3/2}\gamma^{-1/4}\chi^{-3/4}(p, q, r). \quad \text{(B19)}$$

REFERENCES

Batchelor, G. K., 1958: Small-scale variation of convected quantities like temperature in a turbulent fluid. Part 1: General discussion and the case of small conductivity. *J. Fluid Mech.*, **5**, 113–139.

Cessi, P., and W. R. Young, 1992: Multiple equilibria in two-dimensional thermohaline circulation. *J. Fluid Mech.*, **241**, 291–309.

Eckart, C., 1948: An analysis of stirring and mixing processes in incompressible fluids. *J. Mar. Res.*, **7**, 265–275.

Erdogan, M. E., and P. C. Chatwin, 1967: The effects of curvature and buoyancy on the laminar dispersion of solute in a horizontal tube. *J. Fluid Mech.*, **29**, 465–484.

Garrett, C. J. R., 1983: On the initial streakiness of a dispersing tracer in two- and three-dimensional turbulence. *Dyn. Atmos. Oceans*, **7**, 265–277.

Hoskins, B. J., and F. P. Bretherton, 1972: Atmospheric frontogenesis models: Mathematical formulation and solution. *J. Atmos. Sci.*, **29**, 11–37.

Ledwell, J. R., A. J. Watson, and C. S. Law, 1993: Evidence for slow mixing across the pycnocline from an open-ocean tracer-release experiment. *Nature*, **364**, 701–703.

MacVean, M. K., and J. D. Woods, 1980: Redistribution of scalars during upper ocean frontogenesis: A numerical model. *Quart. J. Roy. Meteor. Soc.*, **106**, 293–211.

Roden, G. I., 1977: Oceanic subarctic fronts of the Central Pacific: Structure of and response to atmospheric forcing. *J. Phys. Oceanogr.*, **7**, 761–778.

——, 1986: Thermohaline fronts and baroclinic flows in the Argentine Basin during the austral spring of 1984. *J. Geophys. Res.*, **91**, 5075–5093.

Samelson, R. M., and C. A. Paulson, 1988: Towed thermistor chain observations of fronts in the Subtropical North Pacific. *J. Geophys. Res.*, **93**, 2237–2246.

Smith, R., 1982: Similarity solution of a nonlinear diffusion equation. *Int. Math. Appl. J. Appl. Math.*, **28**, 149–160.

Stommel, H., 1961: Thermohaline convection with two stable regimes of flow. *Tellus*, **13**, 224–230.

——, 1993: A conjectural regulating mechanism for determining the thermohaline structure of the oceanic mixed layer. *J. Phys. Oceanogr.*, **23**, 142–148.

Tandon, A., and C. J. R. Garrett, 1994: Mixed layer restratification due to a horizontal density gradient. *J. Phys. Oceanogr.*, **24**, 1419–1424.

Taylor, G. I., 1953: Dispersion of soluble matter in solvent flowing slowly down a tube. *Proc. Roy. Soc. London Ser. A*, **219**, 186–203.

Young, W. R., 1994: The subinertial mixed layer approximation. *J. Phys. Oceanogr.*, **24**, 1812–1826.

——, and S. Jones, 1991: Shear dispersion. *Phys. Fluids A*, **3**, 1087–1101.

——, P. B. Rhines, and C. J. R. Garrett, 1982: Shear-flow dispersion, internal waves and horizontal mixing in the ocean. *J. Phys. Oceanogr.*, **12**, 515–527.

Yuan, X., and L. D. Talley, 1992: Shallow salinity minimum in the North Pacific. *J. Phys. Oceanogr.*, **22**, 1302–1316.